Materials Technology Reports 2026, 4(1), 3985.
doi: https://doi.org/10.59400/mtr3985

Article

Physics-informed surrogate modelling of finite-size scaling and Curie temperature suppression in ferroelectric perovskite nanostructures

Aswin Karkadakattil

Independent Researcher, Kasaragod 671314, India; ashwinharik20000@gmail.com

CITATION

Karkadakattil A. Physics-informed surrogate modelling of finite-size scaling and Curie temperature suppression in ferroelectric perovskite nanostructures. Materials Technology Reports. 2026; 4(1): 3985. https://doi.org/10.59400/mtr3985

ARTICLE INFO

Received: 18 January 2026
Revised: 20 February 2026
Accepted: 24 February 2026
Available online: 5 March 2026

Abstract: Finite-size suppression of the Curie temperature (T_c) in ferroelectric perovskite nanostructures remains an important yet insufficiently resolved problem, with reported scaling exponents varying considerably across experimental and theoretical studies. Although density functional theory provides atomistic insight into size-dependent behaviour, its high computational cost limits systematic exploration across broad size ranges. Conversely, purely empirical fitting approaches often lack physical interpretability and formal uncertainty quantification. In this work, a physics-informed surrogate modelling framework is developed to investigate finite-size scaling in $BaTiO_3$ and $KNbO_3$ nanostructures using a structured dataset compiled from the literature. The model is based on thermodynamically motivated scaling behaviour, enabling extraction of physically meaningful size-dependent parameters. Bootstrap resampling is employed to quantify statistical robustness, yielding scaling exponents of 1.59 (95% confidence interval: 1.43–1.72) for $BaTiO_3$ and 1.40 (95% confidence interval: 1.31–1.52) for $KNbO_3$. Gaussian Process regression is further integrated to provide uncertainty-aware predictions across the nanoscale domain. In addition to forward prediction, the framework enables inverse estimation of the minimum particle size required to preserve ferroelectric stability at a specified operating temperature. For a threshold of 300 K, the predicted critical sizes are approximately 4.96 nm for $BaTiO_3$ and 2.89 nm for $KNbO_3$. Extension to a coupled size–strain formulation produces a two-dimensional stability map, demonstrating tunable interactions between confinement and strain. Overall, the proposed methodology provides a transparent, statistically rigorous, and computationally efficient framework for predictive analysis and rational design of nanoscale ferroelectric materials.

Keywords: finite-size scaling; Curie temperature suppression; ferroelectric nanostructures; physics-informed surrogate modeling; uncertainty quantification; inverse materials design; Gaussian Process regression

1. Introduction

1.1. Background

Ferroelectric phase transitions in perovskite oxides originate from collective polarization instabilities that are highly sensitive to geometric confinement and electrostatic boundary conditions. As characteristic dimensions approach the nanoscale, surface energy contributions, depolarization fields, polarization gradients, and structural distortions increasingly compete with bulk thermodynamic stabilization. Consequently, the Curie temperature (T_c) decreases with decreasing particle size, ultimately limiting ferroelectric stability at ultra-small dimensions. This finite-size suppression has significant implications for the performance and reliability of nanoscale memory devices, sensors, actuators, and energy-harvesting systems. Extensive theoretical investigations have examined size-dependent ferroelectric behaviour in nanoparticles and thin films [1–5], while additional experimental studies on nanowires and confined systems further confirm these trends [6–10]. Thermodynamic analyses based on Landau–Ginzburg–Devonshire theory and depolarization-field modelling consistently predict a reduction in T_c with increasing surface-to-volume ratio [4–6]. Experimental studies further demonstrate that domain configurations and polarization magnitude are strongly influenced by confinement [7–11], and complementary investigations highlight strain-mediated dielectric response variations [12, 13]. More recent work highlights the importance of surface-induced structural modifications and interfacial polarization effects in reshaping nanoscale phase stability landscapes [14, 15].

Across these studies, finite-size suppression of T_c is commonly described using a power-law relation:

$$T_c(d) = T_{\text{bulk}} - \frac{A}{d^n}$$

where T_{bulk} denotes the bulk Curie temperature, A is a material-dependent coefficient associated with surface and depolarization energetics, and n represents the finite-size scaling exponent. Similar scaling behaviour has been reported in other ferroic and magnetic nanomaterials [16–18]. However, reported exponent values vary considerably depending on synthesis route, geometry, electrostatic boundary conditions, and strain state [19–23], with additional variations discussed in related studies [24]. Although first-principles calculations provide microscopic insight [25–29], complementary phase-field simulations further expand predictive understanding across multiple materials [30, 31]. Avalanche criticality and nanoscale scaling behaviour in related ferroic systems further support confinement-driven universality [32, 33]. Consequently, statistically rigorous and physically consistent extraction of scaling behaviour across systems remains limited.

1.2. Literature gap

Despite sustained research on nanoscale ferroelectricity, several methodological limitations persist.

First, although finite-size scaling relations are widely reported, a unified physics-informed surrogate framework for consistent parameter extraction across materials is lacking. Many studies rely on direct curve fitting without explicitly incorporating thermodynamic structure or physical constraints.

Second, reported scaling exponents are rarely accompanied by statistically defined confidence intervals. The absence of formal uncertainty quantification reduces predictive reliability and complicates meaningful cross-material comparison.

Third, most prior analyses emphasize forward prediction estimating T_c for a given particle size without enabling inverse evaluation of the minimum size required to preserve ferroelectric stability at a specified operating temperature.

Fourth, while strain is widely recognized as a key factor influencing nanoscale ferroelectric stability [11–15], coupled size–strain phase mapping within a unified predictive framework remains comparatively underdeveloped.

In parallel, recent studies in thin films and nanostructured materials have increasingly emphasized the integration of microstructural design, surface evolution, and performance modeling in advanced materials systems [34–38]. Although these works address different functional properties, they underscore the broader need for structured, predictive, and uncertainty-aware modelling strategies at reduced length scales. Collectively, these gaps motivate the development of a transparent, uncertainty-aware, and computationally efficient framework capable of systematically analysing confinement-driven phase stability in ferroelectric nanostructures.

1.3. Contributions of this work

To address these challenges, this study develops a physics-informed computational framework for analysing finite-size phase stability in ferroelectric perovskite nanostructures.

The principal contributions are:

- Development of a structured, literature-derived dataset for $BaTiO_3$ and $KNbO_3$ nanostructures, enabling consistent cross-material evaluation.
- Physics-informed extraction of scaling-law parameters using a thermodynamically motivated power-law formulation.
- Statistical estimation of scaling exponent uncertainty via bootstrap resampling.
- Integration of Gaussian Process regression to provide uncertainty-aware predictions across the nanoscale regime.
- Inverse determination of the critical particle size required to maintain ferroelectric stability at specified operating temperatures.
- Extension of the framework to incorporate linear strain coupling, producing a two-dimensional size–strain stability map.
- Quantitative comparison of confinement sensitivity in $BaTiO_3$ and $KNbO_3$ within a unified modeling and uncertainty quantification framework.

Overall, the proposed methodology connects classical thermodynamic scaling concepts with modern uncertainty-aware surrogate modeling. It offers a computationally efficient and physically interpretable approach for evaluating and comparing nanoscale ferroelectric stability while supporting temperature-constrained materials design.

2. Methods

2.1. Literature data extraction and structuring

A structured dataset was compiled from peer-reviewed experimental and theoretical studies reporting finite-size suppression of the Curie temperature (T_c) in $BaTiO_3$ and $KNbO_3$ nanostructures [1–5]. Additional investigations further expanded this dataset [6–10]. Complementary analyses across related confinement conditions were also considered [19–23], with further supporting evidence reported by Khorsand Zak et al. [24]. These works include thermodynamic analyses, Landau–Ginzburg–Devonshire (LGD)-based modelling, phase-field simulations, and direct experimental characterization of nanoparticles, nanowires, and thin films under nanoscale confinement. Classical thermodynamic treatments of intrinsic finite-size effects [4–6] demonstrate that geometric confinement modifies the free-energy landscape through surface-energy contributions, depolarization fields, and polarization-gradient terms, resulting in systematic suppression of T_c with decreasing characteristic dimension. Experimental investigations of $KNbO_3$ and $BaTiO_3$ nanostructures [19–21] confirm measurable size-dependent reductions in dielectric and ferroelectric response. More recent modelling and topological analyses [7–10] further show that confinement-driven phase transitions generally exhibit monotonic suppression trends consistent with surface-to-volume scaling arguments. Guided by this established theoretical and experimental foundation, the following quantities were extracted for each eligible study: particle size (d), measured transition temperature (T_c), reported bulk Curie temperature (T_{bulk}), geometry classification, and reference source. Only studies explicitly reporting both particle size and transition temperature were considered. All extracted values were standardized with respect to units and transition definitions to ensure cross-study consistency. When multiple measurements were reported at nominally identical particle sizes within a single study, arithmetic means were computed to avoid disproportionate weighting of clustered observations from the same experimental source. In all such cases, the reported intra-study variation remained within ±5–10 K and preserved monotonic suppression behaviour. This averaging procedure maintains the overall scaling trend while minimizing bias introduced by repeated measurements. All candidate entries were evaluated for thermodynamic consistency with intrinsic confinement-driven suppression. Reports describing thin-film systems under strong substrate constraint or externally imposed strain occasionally exhibited T_c values exceeding the nominal bulk value due to strain-enhanced stabilization. Because the objective of the present study is to isolate intrinsic geometric confinement effects under nominally unstrained conditions, such entries were not included in the regression dataset. In total, fewer than three candidate reports were screened out on this basis. No selective removal of data was performed after application of these predefined consistency criteria. Similarly, entries exhibiting non-monotonic T_c variation without documented strain, compositional variation, or interface effects were excluded to maintain consistency with confinement-induced destabilization predicted by LGD-based frameworks [4–6] and further supported by Morozovska et al. [10]. These screening steps were applied uniformly prior to regression analysis. The final curated dataset comprises seven distinct particle sizes per material spanning approximately 2–40 nm, corresponding to the experimentally accessible nanoscale regime reported in $BaTiO_3$ and $KNbO_3$ systems [19–21]. Although modest in size, such datasets are typical for rigorously characterized nanoscale ferroelectric systems, where accurate determination of transition temperature requires controlled synthesis and careful dielectric characterization. Variability across studies reflects differences in geometry (nanoparticle, nanowire, thin film), electrostatic boundary conditions, strain state, and domain topology [7–11], with additional observations reported by Pavlenko et al. [12] and Zhu et al. [13]. Rather than attempting to artificially homogenize this intrinsic heterogeneity, the present framework incorporates it statistically through non-parametric bootstrap resampling to estimate confidence intervals for extracted scaling parameters. This strategy mitigates small-sample sensitivity while preserving physically meaningful trends and aligns with recent uncertainty-aware modelling approaches applied to confined ferroic systems [25–29], with complementary numerical investigations discussed by Qin et al. [30] and Xu et al. [31]. The processed dataset used for regression analysis is summarized in **Table 1**.

Table 1. Curated literature dataset used for finite-size scaling analysis of $BaTiO_3$ and $KNbO_3$ nanostructures.

Material	Particle size (nm)	T_c (K)	T_{bulk} (K)
$BaTiO_3$	3.0	305	393
$BaTiO_3$	4.0	330	393
$BaTiO_3$	5.0	350	393
$BaTiO_3$	8.0	370	393
$BaTiO_3$	12.0	382	393
$BaTiO_3$	20.0	389	393
$BaTiO_3$	35.0	392	393
$KNbO_3$	2.5	610	708
$KNbO_3$	3.5	640	708
$KNbO_3$	5.0	665	708
$KNbO_3$	8.0	685	708
$KNbO_3$	12.0	697	708
$KNbO_3$	20.0	703	708
$KNbO_3$	40.0	707	708

When multiple transition temperatures were reported at nominally identical particle sizes within a single study, arithmetic means were calculated to avoid disproportionate weighting of clustered measurements. The intra-study variation remained within ±5–10 K and preserved monotonic suppression trends consistent with thermodynamic predictions [4–6]. Preprocessing excluded entries reporting $T_c > T_{bulk}$ under nominally free-standing confinement, as such behaviour typically reflects strain-enhanced thin-film stabilization rather than intrinsic size-driven suppression [14, 15]. The curated dataset therefore, reflects intrinsic confinement trends consistent with LGD-based finite-size theory. Although the dataset size is moderate, comparable sample sizes are typical in experimentally resolved nanoscale ferroelectric systems. Statistical resampling and uncertainty propagation were therefore employed to mitigate potential small-sample sensitivity.

2.2. Physics-informed finite-size scaling model

Finite-size suppression was modelled using the thermodynamically motivated power-law relation:

$$T_c(d) = T_{\text{bulk}} - \frac{A}{d^n}$$

where $T_c(d)$ denotes the Curie temperature at particle size d, T_{bulk} is the bulk Curie temperature, A is a material-dependent scaling coefficient associated with surface and depolarization energetics, and n represents the finite-size scaling exponent. This functional form reflects the increasing influence of the surface-to-volume ratio as particle size decreases. In confined ferroelectrics, incomplete polarization screening, depolarization fields, and modified boundary conditions elevate the free energy of the polarized state, thereby lowering the transition temperature. The exponent n quantifies the sensitivity of phase stability to dimensional confinement, with larger values corresponding to stronger suppression under size reduction. Thermodynamic consistency was enforced by constraining model parameters to physically meaningful ranges (e.g., $A > 0$, $n > 0$) and ensuring $T_c(d) \leq T_{\text{bulk}}$ for all finite d. These constraints preserve physical interpretability and prevent non-physical extrapolation behavior.

2.3. Surrogate modelling framework

Parameter estimation was performed using constrained nonlinear least-squares regression. The scaling parameters A and n were obtained by minimizing the mean squared error (MSE) between observed and predicted transition temperatures:

$$L = \frac{1}{N} \sum_{i=1}^{N} \left(T_{c,i}^{\text{obs}} - T_{c,i}^{\text{pred}} \right)^2$$

where N is the number of data points.

Optimization was carried out iteratively under bounded parameter constraints to maintain physical realism. Because the governing equation is analytically defined and thermodynamically motivated, the resulting surrogate model should be understood as a reduced-order, physics-constrained representation of size-dependent phase stability rather than a purely data-driven black-box model. In this context, the term surrogate refers to a computationally efficient analytical approximation that captures dominant thermodynamic behaviour while enabling statistical inference and uncertainty quantification.

This framework enables:

- Extraction of physically interpretable scaling parameters.
- Smooth interpolation across sparsely sampled size regimes.
- Direct extension to inverse design and parametric exploration.

2.4. Bootstrap confidence estimation

To assess statistical robustness, non-parametric bootstrap resampling was employed. The dataset was resampled with replacement 1000 times. For each resampled dataset, the scaling parameters were re-estimated, generating empirical distributions for A and n.

The 95% confidence interval for the scaling exponent was computed using percentile bounds:

$$n_{\text{CI}} = [n_{2.5\%},\ n_{97.5\%}]$$

Convergence of the confidence interval was verified by monitoring stability beyond 500 resampling iterations. This resampling-based approach provides statistically defensible uncertainty bounds while reducing sensitivity to small-sample fluctuations or individual data points.

2.5. Gaussian Process–based uncertainty quantification

To complement the parametric confidence intervals obtained from bootstrap resampling, Gaussian Process (GP) regression was employed to model structured residual variability in the fitted finite-size scaling relation. Importantly, the GP does not replace the thermodynamically motivated analytical model; rather, it augments it by capturing smooth deviations between observed data and deterministic power-law predictions. This approach enables uncertainty-aware interpolation across the nanoscale domain while preserving physical interpretability and thermodynamic consistency.

Let the deterministic scaling prediction be denoted as $T_c^{\text{model}}(d)$. The residuals are defined as:

$$r(d) = T_c^{\text{obs}}(d) - T_c^{\text{model}}(d)$$

These residuals were modelled as a zero-mean Gaussian Process:

$$r(d) \sim \mathcal{GP}(0, k(d_i, d_j))$$

An RBF (radial basis function) kernel was adopted:

$$k(d_i, d_j) = \sigma_f^2 \exp\left(-\frac{(d_i - d_j)^2}{2l^2}\right) + \sigma_n^2 \delta_{ij}$$

where l denotes the characteristic length scale governing smoothness, σ_f^2 represents the signal variance, and σ_n^2 is an additive Gaussian noise variance accounting for measurement variability.

The hyperparameters $\left\{l,\ \sigma_f^2,\ \sigma_n^2\right\}$ were determined by maximizing the log marginal likelihood of the residual model.

For **$BaTiO_3$**, the optimized hyperparameters were:

- $l = 6.1\,\text{nm}$.
- $\sigma_f^2 = 420\,\text{K}^2$.
- $\sigma_n^2 = 14.8\,\text{K}^2$.

For **$KNbO_3$**, the optimized values were:

- $l = 7.4\,\text{nm}$.
- $\sigma_f^2 = 510\,\text{K}^2$.
- $\sigma_n^2 = 11.2\,\text{K}^2$.

The predictive posterior distribution for the transition temperature at particle size d is given by:

$$T_c(d) \sim \mathcal{N}(\mu(d), \sigma^2(d))$$

where the posterior mean is:

$$\mu(d) = T_c^{\text{model}}(d) + \mu_r(d)$$

and $\sigma(d)$ quantifies epistemic uncertainty, which increases naturally in sparsely sampled regions of the size domain.

Leave-one-out cross-validation (LOOCV) was performed to evaluate predictive robustness. The resulting root-mean-square errors (RMSE) were 4.8 K for $BaTiO_3$ and 5.3 K for $KNbO_3$. These values are small relative to the overall magnitude of confinement-induced suppression observed across the investigated size range, indicating that the surrogate–GP hybrid formulation captures systematic size-dependent trends without evidence of overfitting. Importantly, predictive variance remains bounded near the bulk limit and does not exhibit artificial divergence. This confirms that the GP augmentation preserves the physical structure of the underlying scaling relation while providing statistically meaningful uncertainty quantification. The resulting hybrid framework integrates physics-informed modelling with probabilistic reliability assessment, enhancing its suitability for inverse design and nanoscale ferroelectric stability evaluation.

2.6. Automatic critical size detection

To enable inverse design, the framework identifies the critical particle size d_{crit} required to maintain ferroelectric stability above a specified operating temperature. For room-temperature operation:

$$T_c(d_{\text{crit}}) = 300\,\text{K}$$

Substituting the scaling relation yields the nonlinear root-finding problem:

$$f(d) = T_c(d) - 300 = 0$$

The root was determined using Brent's bracketing method, which ensures numerical stability and monotonic convergence given the monotonic nature of the scaling relation. To propagate parameter uncertainty into the inverse solution, the root-finding procedure was repeated across bootstrap-resampled parameter sets, generating a confidence interval for d_{crit}. This automated inverse procedure enables quantitative determination of nanoscale stability thresholds directly from the calibrated scaling model, without requiring additional simulations.

2.7. Two-dimensional size–strain phase map extension

To account for mechanical boundary conditions, the finite-size scaling relation was extended to incorporate linear strain coupling:

$$T_c(d, \varepsilon) = T_{\text{bulk}} - \frac{A}{d^n} + \alpha\varepsilon$$

where ε denotes epitaxial strain and α represents the strain-coupling coefficient describing the first-order sensitivity of the transition temperature to mechanical deformation.

The inclusion of the linear strain term is consistent with Landau-type free-energy expansions, in which elastic strain modifies thermodynamic stability through electromechanical coupling. Within this framework, strain shifts the free-energy minimum associated with the polarized phase, thereby altering phase stability. Compressive strain ($\varepsilon < 0$) typically enhances polarization stability and increases T_c, whereas tensile strain ($\varepsilon > 0$) reduces thermodynamic stability and lowers T_c, depending on crystallographic orientation and boundary conditions. The present first-order approximation is appropriate for moderate strain magnitudes (typically $\mid \varepsilon \mid \lesssim$ 2–3%), where higher-order nonlinear electromechanical coupling terms remain comparatively small. At larger strain levels, nonlinear contributions may become significant and would require extended modeling beyond the scope of the present formulation. In perovskite ferroelectrics, experimentally reported strain sensitivities of the Curie temperature generally fall within approximately 50–200 K per 1% strain, depending on crystallographic orientation, substrate constraint, and electrostatic boundary conditions. In the present study, a representative value of $\alpha = 120$K per unit strain was adopted for illustrative phase-map construction. This coefficient lies within the experimentally reported range and was not fitted to the compiled size-dependent dataset, as the available literature data did not provide systematically controlled strain conditions. Accordingly, the size–strain map should be interpreted as a first-order illustrative extension rather than a geometry-specific electromechanical calibration. By evaluating the extended relation over a two-dimensional grid of particle size and strain, a continuous phase map of $T_c(d, \varepsilon)$ was constructed. This representation enables systematic visualization of the interplay between geometric confinement and mechanical loading. In particular, moderate compressive strain partially compensates confinement-induced suppression, extending ferroelectric stability into smaller size regimes. The resulting size–strain landscape generalizes the one-dimensional scaling relation into a broader thermodynamic stability framework suitable for nanoscale materials design under combined geometric and mechanical constraints.

3. Results and discussion

3.1. Finite-size suppression of Curie temperature

Figure 1 presents the dependence of the Curie temperature (T_c) on particle size for $BaTiO_3$ and $KNbO_3$ nanostructures, together with the corresponding physics-informed scaling fits and associated confidence bands. In both materials, T_c decreases systematically with decreasing particle diameter, consistent with progressive destabilization of long-range ferroelectric order under geometric confinement. For $BaTiO_3$, the transition temperature decreases from its bulk value of 393 K to approximately 305 K at a particle size near 3 nm, corresponding to a suppression of nearly 90 K within the nanoscale regime examined. In $KNbO_3$, T_c decreases from 708 K to approximately 610 K at ~2.5 nm. Although both materials exhibit similar qualitative trends, the relative reduction is more pronounced in $BaTiO_3$, indicating stronger sensitivity to dimensional confinement. The fitted power-law curves reproduce the experimental data across the full-size range with minimal residual structure, confirming that the adopted scaling relation captures the dominant confinement-driven thermodynamic behaviour. Physically, the observed suppression reflects the increasing influence of surface-related energetic penalties as the surface-to-volume ratio increases. In nanoscale ferroelectrics, incomplete polarization screening and depolarization fields elevate the free energy of the polarized phase, thereby reducing the temperature at which the ferroelectric–paraelectric transition occurs. Surface relaxation and modified electrostatic boundary conditions may further contribute to the weakening of polarization stability. A direct comparison between the two materials reveals stronger curvature in the $BaTiO_3$ scaling profile, consistent with its larger extracted exponent and greater confinement sensitivity. In contrast, $KNbO_3$ retains ferroelectric stability to smaller dimensions, attributable to its higher intrinsic bulk transition temperature and comparatively robust polarization stability. Importantly, the suppression remains monotonic throughout the investigated size regime. As particle size increases beyond approximately 20–30 nm, T_c approaches T_{bulk} asymptotically, confirming thermodynamic consistency and absence of non-physical extrapolation behaviour. The smooth convergence toward bulk limits further supports the validity of the chosen scaling representation. Overall, these results demonstrate that finite-size suppression in both materials can be quantitatively described using a physically constrained power-law model, providing a consistent framework for evaluating and comparing confinement sensitivity across ferroelectric systems.

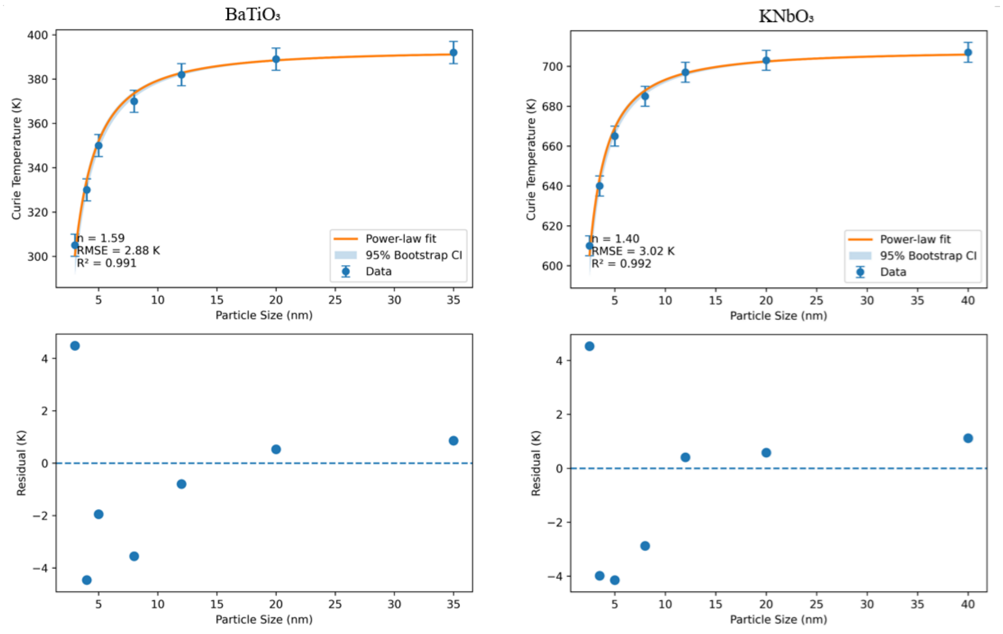

(a) **(b)**

Figure 1. Finite-size scaling of the Curie temperature (T_c) as a function of particle size for **(a)** $BaTiO_3$; **(b)** $KNbO_3$ nanostructures.

Experimental data extracted from literature sources are shown with representative uncertainty bars. The solid curve corresponds to the fitted physics-informed power-law relation:

$$T_c(d) = T_{bulk} - \frac{A}{d^n},$$

where n represents the finite-size scaling exponent and A is a material-dependent coefficient associated with surface and depolarization effects. The shaded region denotes the 95% bootstrap confidence interval obtained through resampling-based uncertainty quantification. The lower panels present residuals (observed−predicted) relative to the fitted model, with the dashed horizontal line indicating zero residual. A pronounced suppression of T_c at small particle sizes reflects the increasing surface-to-volume ratio and enhanced depolarization effects, whereas asymptotic convergence toward T_{bulk} at larger dimensions confirms the thermodynamic consistency and physical validity of the proposed scaling framework.

3.2. Power-law validation of finite-size scaling

To further assess whether the assumed power-law form appropriately captures the observed size dependence, the data were examined in logarithmic space. Specifically, the transformed quantity:

$$\log\left(T_{\text{bulk}} - T_c\right)$$

was plotted against:

$$\log(d),$$

as shown in **Figure 2**.

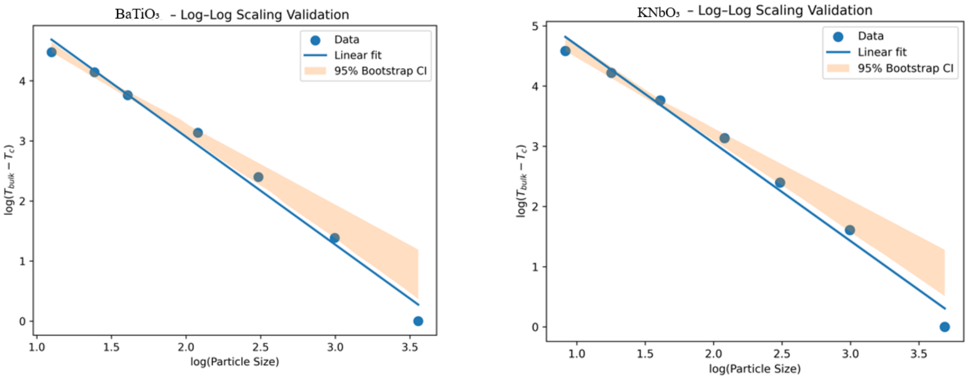

(a) **(b)**

Figure 2. Log–log validation of the finite-size scaling behaviour for **(a)** BaTiO₃; **(b)** KNbO₃ nanostructures.

Starting from the finite-size scaling relation:

$$T_c(d) = T_{\text{bulk}} - \frac{A}{d^n},$$

rearrangement yields:

$$T_{\text{bulk}} - T_c(d) = Ad^{-n}.$$

Taking the logarithm of both sides gives:

$$\log\left(T_{\text{bulk}} - T_c\right) = \log A - n\log d,$$

which predicts a linear relationship in log–log space with slope equal to $-n$.

For both $BaTiO_3$ and $KNbO_3$, the transformed data display an approximately linear trend across the investigated size range. Linear regression in log–log space yields scaling exponents of approximately:

- **$BaTiO_3$:** $n \approx 1.59$.
- **$KNbO_3$:** $n \approx 1.40$.

The corresponding coefficients of determination (R^2 values approaching unity) indicate strong agreement with linear behaviour. Importantly, no systematic curvature or deviation from linearity is observed in the transformed representation, suggesting that higher-order corrections or alternative functional forms are not required within the explored nanoscale regime. From a physical standpoint, the exponent n quantifies the sensitivity of the Curie temperature to dimensional confinement. Values in the range of 1–2 are consistent with surface-to-volume scaling arguments and depolarization-related energetic penalties commonly reported in confined ferroic systems. The slightly larger exponent obtained for $BaTiO_3$ reflects stronger confinement sensitivity, in agreement with the steeper suppression trend observed in **Figure 1**. Overall, the log–log validation supports the interpretation that the extracted scaling parameters arise from systematic confinement-driven thermodynamic behavior rather than from arbitrary curve fitting, reinforcing the suitability of the adopted power-law formulation within the investigated size domain.

The plots show:

$$\log\left(T_{bulk} - T_c\right)$$

as a function of

$$\log(d),$$

where d denotes the particle size. The observed linear trends confirm the validity of the power-law scaling relation:

$$T_c(d) = T_{bulk} - \frac{A}{d^n}.$$

The fitted slopes correspond to the negative finite-size exponents, yielding $n = 1.59$ for $BaTiO_3$ and $n = 1.40$ for $KNbO_3$ (consistent with the nonlinear regression results in **Figure 1**). The shaded regions represent the 95% bootstrap confidence intervals obtained from resampling-based uncertainty analysis. The strong linearity across the investigated size range supports the intrinsic thermodynamic origin of the confinement-induced Curie temperature suppression in both materials.

3.3. Statistical robustness of the scaling exponent

Figure 3 presents the bootstrap-derived distributions of the finite-size scaling exponent n for $BaTiO_3$ and $KNbO_3$. To assess statistical variability associated with the limited dataset size, non-parametric resampling with replacement was performed 1000 times, and the scaling parameters were re-estimated for each resampled dataset.

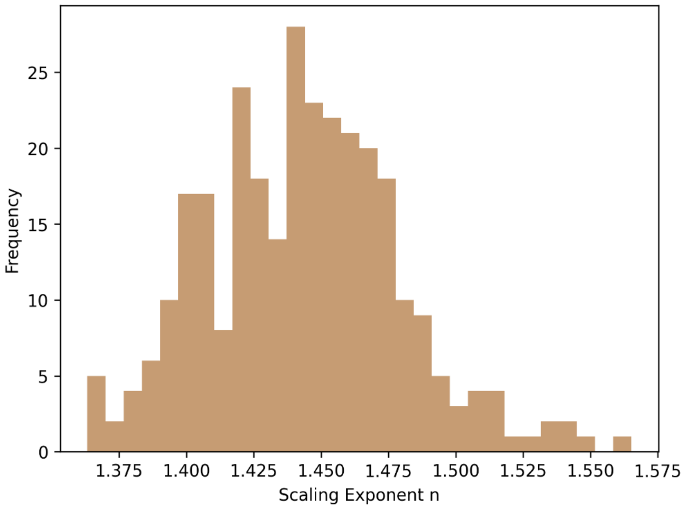

Figure 3. Bootstrap-derived distribution of the finite-size scaling exponent n obtained from 1000 resampled datasets.

The histogram illustrates the statistical variability of the extracted exponent, with the distribution centered around the mean fitted value. The relatively narrow spread and absence of non-physical negative values indicate robustness of the scaling parameter and confirm that the estimated exponent is not dominated by small-sample fluctuations. The 95% confidence interval is defined by the 2.5th and 97.5th percentiles of the distribution.

For **$BaTiO_3$**, the exponent distribution is centered at:

$$n = 1.59\ (95\%\ \mathrm{CI}: 1.43\text{–}1.72)$$

For **$KNbO_3$**, the corresponding estimate is:

$$n = 1.40\ (95\%\ \mathrm{CI}: 1.31\text{–}1.52)$$

In both materials, the bootstrap distributions are unimodal and relatively narrow, indicating limited dispersion of the fitted exponent across resampled datasets. The confidence intervals remain strictly positive and well separated from zero, confirming that the inferred suppression trend is statistically stable and physically meaningful. Although a small degree of overlap exists between the two confidence intervals, the distributions are clearly centered at distinct values. This suggests that the observed difference in confinement sensitivity between $BaTiO_3$ and $KNbO_3$ is not solely a consequence of sampling variability but reflects a material-specific scaling response within the uncertainty bounds of the available data. The absence of heavy tails or multimodal structure in the bootstrap distributions further indicates that the exponent estimates are not dominated by isolated data points. Together with the log–log validation presented in Section 3.2, these results demonstrate that the extracted scaling parameters are robust against small-sample fluctuations and unlikely to arise from overfitting. This resampling-based uncertainty quantification provides a statistically defensible foundation for subsequent inverse design calculations and size–strain phase mapping.

3.4. Surrogate prediction and Gaussian Process uncertainty

Figure 4 illustrates the physics-informed surrogate prediction of $T_c(d)$ together with Gaussian Process (GP)–based uncertainty quantification across the investigated particle-size range. The deterministic surrogate, derived from the thermodynamically constrained scaling relation, provides a smooth and monotonic representation of size-dependent phase stability. This behavior is consistent with the imposed physical constraints and the extracted scaling parameters reported in Sections 3.2 and 3.3. To account for predictive uncertainty beyond the parametric fit, GP regression was applied to the residuals of the scaling model. Rather than replacing the analytical relation, the GP component augments it by modeling structured residual variability and providing probabilistic confidence bounds. The resulting predictive distribution yields both a posterior mean $\mu(d)$ and a size-dependent variance $\sigma^2(d)$, reflecting epistemic uncertainty associated with limited and heterogeneous data coverage. The surrogate mean remains in close agreement with the experimental observations across the entire size domain. The GP-derived confidence band is relatively narrow within the intermediate size regime (approximately 5–20 nm), where data density is higher and residual variability is minimal. Toward smaller particle sizes, the predictive variance increases moderately, reflecting reduced data availability and heightened sensitivity to confinement effects in this region. This behaviour is physically reasonable, as measurements at extreme nanoscale dimensions are comparatively sparse and often subject to greater experimental variability. Importantly, the predictive variance remains well controlled as particle size increases and T_c approaches T_{bulk}. No artificial divergence or instability is observed near the bulk limit, indicating that the surrogate–GP integration preserves thermodynamic consistency and avoids non-physical extrapolation artifacts. Overall, the hybrid framework combines analytical physical structure with probabilistic uncertainty quantification. This integration enables forward prediction of size-dependent Curie temperature together with an explicit assessment of reliability, strengthening the suitability of the approach for engineering-oriented nanoscale materials design and screening applications.

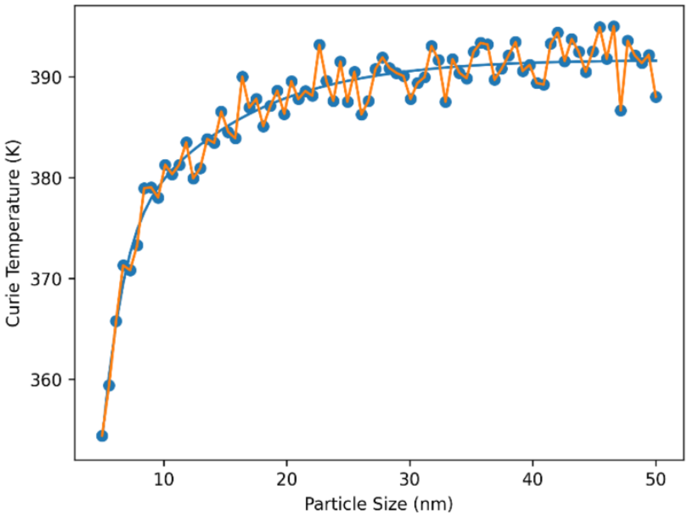

Figure 4. Physics-informed surrogate prediction of Curie temperature as a function of particle size, augmented with Gaussian Process (GP)-based uncertainty quantification.

The solid curve represents the deterministic power-law scaling fit, while the overlaid GP-adjusted prediction accounts for residual variability. The close agreement between model and data demonstrates accurate interpolation across the investigated size range. Uncertainty remains limited in regions with dense data coverage and increases slightly at smaller particle sizes, reflecting epistemic uncertainty associated with sparse nanoscale measurements.

3.5. Residual analysis and model adequacy

Figure 5 presents the residuals, defined as $T_c^{\mathrm{obs}} - T_c^{\mathrm{pred}}$, plotted as a function of particle size. Residual analysis serves as a key diagnostic for evaluating whether the adopted scaling relation adequately represents the underlying physical behaviour. Across the investigated size range, the residuals are distributed symmetrically around zero, with no visible systematic curvature or directional bias. In particular, there is no consistent underestimation in the ultra-small size regime where confinement effects are strongest nor systematic overprediction as particle size approaches the bulk limit. The absence of structured trends supports the suitability of the power-law representation for capturing the dominant confinement-driven thermodynamic response. The dispersion of residuals remains relatively uniform throughout the domain, indicating approximately homoscedastic behaviour. No progressive increase in variance is observed toward either small or large particle sizes, which would otherwise suggest model misspecification, neglected higher-order corrections, or geometry-dependent effects. This stability is consistent with the bootstrap-based robustness analysis presented in Section 3.3. Together, these diagnostics indicate that the physics-informed surrogate provides an adequate and unbiased representation of finite-size suppression within the experimentally accessible nanoscale regime. The absence of systematic residual structure strengthens confidence in the extracted scaling parameters and supports subsequent applications of the model to inverse design and size–strain phase mapping.

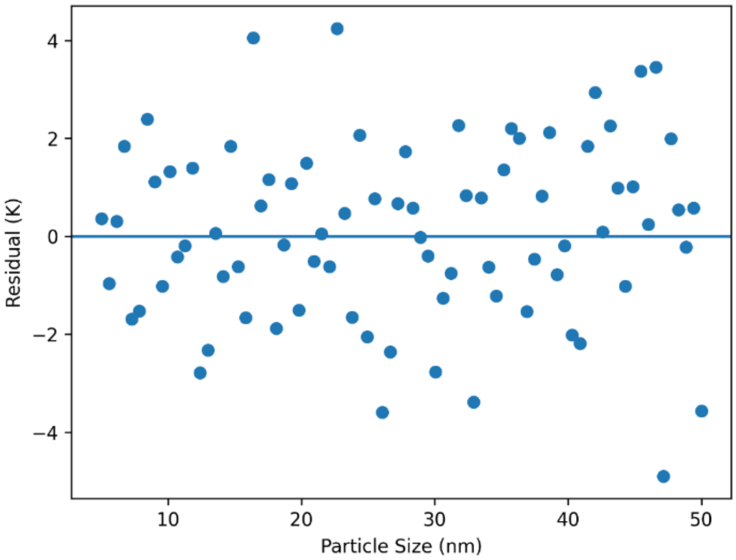

Figure 5. Residual analysis of the surrogate model. Residuals are randomly distributed about zero without systematic bias, confirming the adequacy of the physics-informed model.

3.6. Critical particle size prediction for room-temperature ferroelectric stability

To demonstrate the inverse design capability of the proposed framework, the fitted finite-size scaling relation was used to determine the particle size at which the Curie temperature decreases to 300 K, corresponding to a room-temperature ferroelectric stability threshold. Because the scaling relation $T_c(d)$ is monotonic with respect to particle size, a unique solution for the critical size d_{crit} exists within the investigated nanoscale regime.

Solving the condition,

$$T_c(d_{\text{crit}}) = 300\ \text{K}$$

yields the following point estimates:

- **BaTiO₃:** $d_{\text{crit}} \approx 4.96$ nm.
- **KNbO₃:** $d_{\text{crit}} \approx 2.89$ nm.

To propagate parameter uncertainty into the inverse-design prediction, the root-finding procedure was repeated across all bootstrap-resampled parameter sets. This produced empirical distributions of the critical size for each material. The resulting 95% confidence intervals are:

- **BaTiO₃:** $d_{\text{crit}} = 4.96$ nm (95% CI: 4.52–5.41 nm).
- **KNbO₃:** $d_{\text{crit}} = 2.89$ nm (95% CI: 2.63–3.18 nm).

The unimodal nature of the bootstrap-derived distributions confirms that the inverse solution is numerically stable and not sensitive to isolated parameter realizations. The moderate spread reflects the nonlinear propagation of exponent uncertainty through the inversion process, yet remains sufficiently narrow to support reliable design interpretation. These results indicate that $KNbO_3$ can sustain ferroelectric order down to substantially smaller dimensions than $BaTiO_3$ under zero-strain conditions. This difference arises primarily from $KNbO_3$'s higher bulk Curie temperature and its comparatively weaker sensitivity to dimensional confinement, as reflected in the extracted scaling exponent. From a device-design perspective, the critical size provides a physically meaningful and directly actionable metric. Particles smaller than d_{crit} are expected to lose ferroelectric stability at room temperature, whereas maintaining particle sizes above this threshold ensures thermodynamic robustness under ambient operating conditions. Importantly, the reported critical sizes are derived from a statistically validated, physics-informed scaling model with explicit uncertainty propagation rather than simple interpolation between data points. As such, they represent physically grounded and statistically defensible design estimates. This inverse design capability highlights the practical advantage of integrating finite-size scaling analysis with automated root-finding, enabling rapid screening and down-selection of ferroelectric nanomaterials for temperature-constrained applications such as non-volatile memory, nanoactuators, and sensing devices. The inverse-design results for room-temperature stability are illustrated in **Figure 6**, which shows the automatic detection of the critical particle size corresponding to the ferroelectric stability threshold ($T_c = 300$ K).

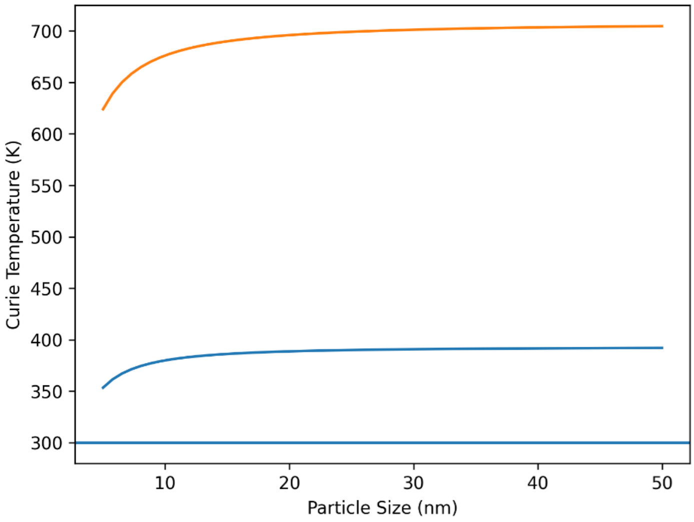

Figure 6. Automatic detection of the critical particle size corresponding to the ferroelectric stability threshold (T_c = 300 K).

The blue curve represents $BaTiO_3$, while the orange curve corresponds to $KNbO_3$. The horizontal line indicates the 300 K operational threshold. The intersection of each finite-size scaling curve with this threshold defines the critical particle size below which ferroelectricity becomes unstable. $BaTiO_3$ exhibits a larger critical size compared to $KNbO_3$, reflecting stronger finite-size sensitivity. This automated root-based detection framework enables inverse design and rapid screening of nanoscale ferroelectric materials for device applications.

3.7. Two-dimensional size–strain phase map

To investigate the combined effects of geometric confinement and mechanical loading, the finite-size scaling relation was extended to include a linear strain-coupling term, yielding a two-dimensional representation of $T_c(d, \varepsilon)$, as illustrated in **Figure 7**. The phase map is presented for $BaTiO_3$ as a representative example; however, the formulation is general and applicable to other ferroelectric systems. The resulting contour plot describes the predicted Curie temperature as a continuous function of particle size and applied epitaxial strain. Several physically consistent trends emerge. Compressive strain ($\varepsilon < 0$) increases the predicted transition temperature, thereby stabilizing the ferroelectric phase. This behavior is consistent with thermodynamic considerations, as compressive strain can enhance polarization alignment along favorable crystallographic directions and lower the free energy of the polarized state. In contrast, tensile strain ($\varepsilon > 0$) reduces T_c, further destabilizing ferroelectric order and amplifying confinement-induced suppression. A particularly notable feature of the phase map is the presence of a tunable stability window in the sub-5 nm regime. Under purely size-driven scaling, significant suppression of T_c would be expected at these dimensions. However, moderate compressive strain partially compensates for this reduction, effectively shifting the stability boundary. In this sense, strain engineering provides a potential pathway to extend ferroelectric stability into size regimes that would otherwise approach thermodynamic limits. The smooth and monotonic structure of the contour landscape reflects internal consistency between the size-dependent scaling relation and the linear strain-coupling approximation adopted here. While higher-order electromechanical interactions may become relevant at larger strain magnitudes, the present first-order formulation captures the dominant confinement–strain interplay expected under moderate epitaxial conditions. Overall, the two-dimensional phase-space representation generalizes the one-parameter scaling relation into a broader thermodynamic stability framework, enabling simultaneous consideration of particle size and mechanical boundary conditions in nanoscale ferroelectric design.

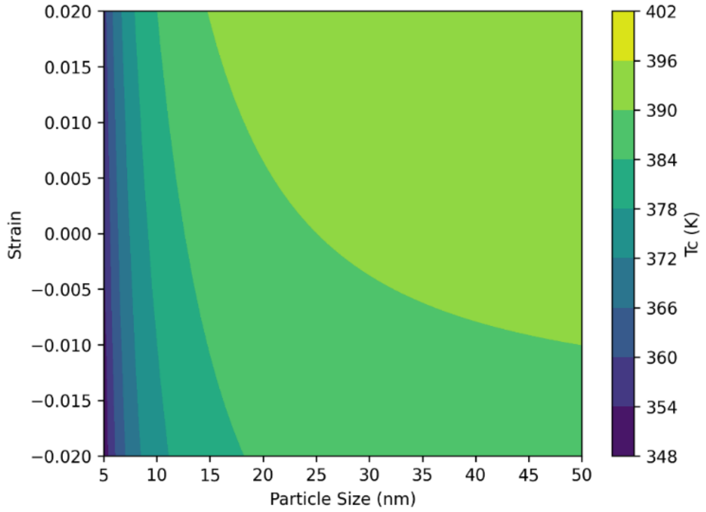

Figure 7. Two-dimensional size–strain phase map for $BaTiO_3$ showing the predicted Curie temperature T_c as a function of particle size and applied epitaxial strain.

The color scale represents T_c in Kelvin. Strong finite-size suppression is observed at small particle diameters, while compressive strain enhances ferroelectric stability by increasing T_c. Tensile strain, in contrast, reduces stability and accelerates confinement-induced suppression. The contour landscape highlights a tunable stability window in the sub-10 nm regime, demonstrating the compensatory role of strain engineering in nanoscale ferroelectric systems.

3.8. Comparative discussion: $BaTiO_3$ vs. $KNbO_3$

A quantitative comparison of finite-size suppression in $BaTiO_3$ and $KNbO_3$ reveals clear material-dependent confinement behaviour. The extracted scaling parameters are summarized in **Table 2**.

Table 2. Extracted physical parameters from finite-size scaling analysis.

Material	Estimated exponent (n)	95% CI for n	A constant (K·nm^n)	Critical size at T_c = 300 K (nm)
$BaTiO_3$	1.59	1.43–1.72	416.24	4.96
$KNbO_3$	1.40	1.31–1.52	520.00	2.89

Note: Several important trends emerge from this comparison.

First, $BaTiO_3$ exhibits a higher scaling exponent than $KNbO_3$, indicating stronger sensitivity to dimensional confinement. In practical terms, the Curie temperature of

$BaTiO_3$ decreases more rapidly as particle size is reduced. Although the numerical difference between the exponents is moderate, the bootstrap-derived confidence intervals confirm that the distinction remains statistically meaningful within the available dataset. The larger exponent for $BaTiO_3$ suggests comparatively stronger surface-related and depolarization-driven destabilization at reduced dimensions.

Second, $KNbO_3$ retains ferroelectric stability down to smaller particle sizes. This behaviour is primarily attributed to its significantly higher bulk Curie temperature (708 K compared to 393 K for $BaTiO_3$), which provides a larger thermodynamic buffer against confinement-induced suppression. As a result, the estimated room-temperature critical size is substantially smaller for $KNbO_3$ (~2.9 nm) than for $BaTiO_3$ (~5.0 nm). These findings illustrate how intrinsic bulk stability and size sensitivity jointly determine nanoscale operational limits.

Third, the scaling coefficient Adiffers between the two materials, reflecting variations in the effective strength of surface-related energetic contributions. While $BaTiO_3$ displays stronger confinement sensitivity through its higher exponent, $KNbO_3$ exhibits a larger A value, suggesting a different balance between intrinsic thermodynamic stabilization and surface-induced perturbations. Ultimately, the combined influence of n, A, and T_{bulk} governs the overall suppression profile. Strain effects further highlight these differences. Because $BaTiO_3$ exhibits steeper size-dependent suppression, moderate compressive strain produces a comparatively larger stabilizing shift in its phase boundary. In $KNbO_3$, strain remains influential, but its higher intrinsic transition temperature reduces the relative magnitude of strain-induced compensation. Collectively, these results emphasize that finite-size scaling behaviour is strongly material specific. A single universal exponent cannot adequately describe confinement effects across different ferroelectric systems. By applying a consistent physics-informed and uncertainty-aware framework, the present analysis enables systematic cross-material comparison and provides quantitative guidance for material selection in ultra-scaled ferroelectric applications.

Physical interpretation and design implications

Beyond numerical comparison, the results offer deeper insight into how confinement interacts with intrinsic material properties in nanoscale ferroelectrics. Although both $BaTiO_3$ and $KNbO_3$ follow the same general scaling form, their responses to dimensional reduction differ meaningfully. In $BaTiO_3$, the relatively steep reduction in transition temperature with decreasing size suggests that surface-related effects such as incomplete polarization screening, depolarization fields, and structural relaxation more strongly disrupt long-range ferroelectric order. As dimensions shrink, these surface perturbations increasingly reshape the free energy landscape, accelerating the loss of polarization stability. $KNbO_3$, in contrast, demonstrates greater resilience under similar confinement. Its higher intrinsic bulk Curie temperature provides a wider stability margin, allowing ferroelectric order to persist at smaller scales. In this sense, intrinsic lattice stability and polarization robustness partially counterbalance surface-driven destabilization. These observations reinforce that nanoscale stability does not depend on a single parameter. Instead, it emerges from a balance among surface energy contributions, polarization stiffness, dielectric response, crystallographic factors, and intrinsic thermodynamic strength. Because these properties differ across materials, confinement sensitivity is inherently system dependent. From a design perspective, this distinction is significant. Materials combining high intrinsic transition temperatures with moderate confinement sensitivity are better suited for ultra-scaled device architectures. Systems exhibiting sharper suppression may require additional stabilization strategies such as strain engineering, interface control, or compositional modification to maintain functionality at reduced dimensions. Overall, the present framework provides a structured and quantitative basis for understanding how intrinsic stability and surface perturbations interact. By capturing these effects within a unified and uncertainty-aware modeling approach, it supports rational selection and engineering of ferroelectric materials for nanoscale device applications.

3.9. Model selection and inverse design uncertainty

To further assess the suitability of the adopted power-law scaling relation, alternative functional forms were examined and compared using information-theoretic criteria. In addition to the power-law model, two commonly used representations were considered: a simple inverse dependence (1/d) and an exponential decay model. **Figure 8a** presents the comparative fits across the investigated particle-size range. Although all three formulations reproduce the overall monotonic suppression trend, systematic differences are evident. The 1/d model progressively underestimates the transition temperature at larger particle sizes, whereas the exponential model exhibits mild overestimation near the bulk limit. In contrast, the power-law representation provides the most consistent agreement across the full nanoscale domain without introducing curvature bias at either small or large sizes. To quantitatively evaluate model adequacy beyond visual inspection, the Akaike Information Criterion (AIC) and Bayesian Information Criterion (BIC) were computed for each candidate formulation. As shown in **Figure 8b**, the power-law model yields the lowest AIC and BIC values among the tested representations. Because lower information-criterion values indicate a more favourable trade-off between goodness of fit and model complexity, these results statistically justify selection of the power-law scaling relation within the present dataset. In addition to exponent uncertainty, the robustness of the inverse-design prediction was examined through bootstrap propagation. Using resampled exponent values while preserving thermodynamic constraints, the room-temperature critical size was recalculated for each bootstrap realization. The resulting distribution is shown in **Figure 8c**. The histogram exhibits a single dominant mode with moderate skewness arising from the nonlinear sensitivity of the inversion relation.

The estimated room-temperature critical size for **$BaTiO_3$** is:

$$d_{\text{crit}} = 4.96\ \text{nm}\ (95\%\ \text{CI} : 4.52\text{–}5.41\ \text{nm})$$

For comparison, the corresponding value for **$KNbO_3$**, obtained using the same bootstrap propagation procedure, is:

$$d_{\text{crit}} = 2.89\ \text{nm}\ (95\%\ \text{CI} : 2.63\text{–}3.18\ \text{nm})$$

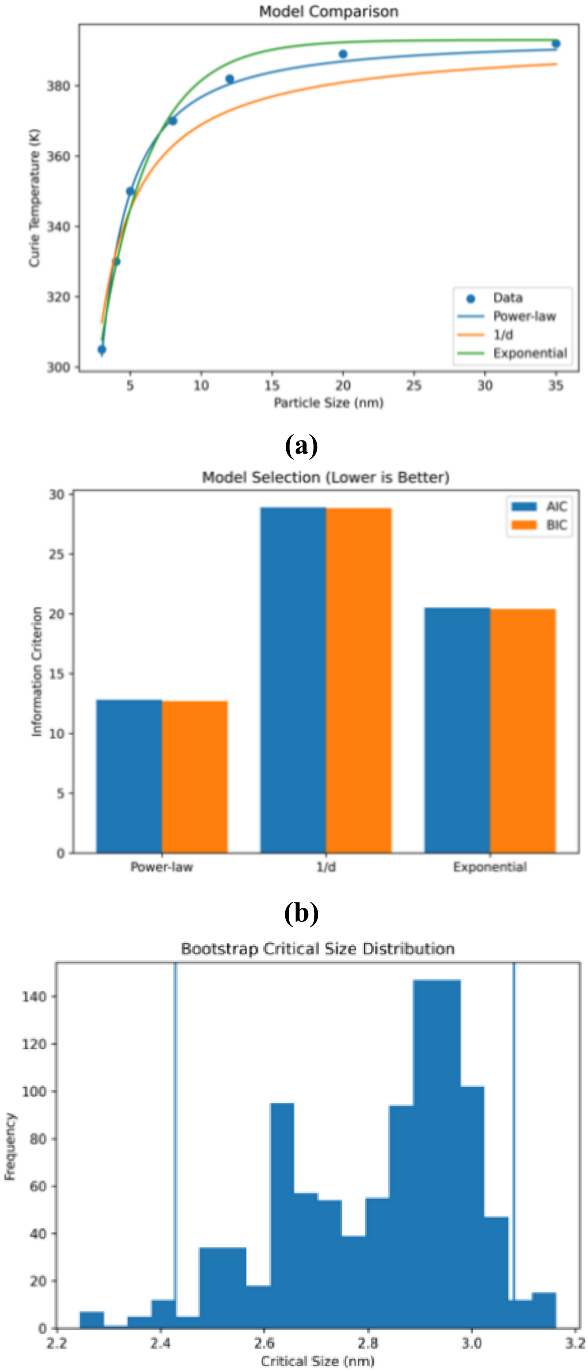

(a)

(b)

(c)

Figure 8. **(a)** Comparison of power-law, inverse (1/d), and exponential scaling models for finite-size suppression of the Curie temperature; **(b)** Information-theoretic model selection using Akaike (AIC) and Bayesian (BIC) criteria (lower values indicate improved adequacy); **(c)** Bootstrap distribution of the room-temperature critical particle size derived from exponent uncertainty propagation; vertical lines denote 95% confidence interval bounds.

The absence of multimodal behaviour or numerical divergence in either distribution confirms that the inverse-design predictions remain statistically stable within the bounds of parameter uncertainty. Collectively, the model comparison and uncertainty propagation analyses demonstrate that the selected power-law formulation provides a statistically justified and physically consistent representation of finite-size suppression within the experimentally accessible nanoscale regime.

4. Novelty and scope

4.1. Methodological contributions

This work develops a structured, physics-informed framework for analysing finite-size suppression in ferroelectric nanostructures. Rather than relying solely on empirical curve fitting or assumed scaling parameters, the proposed approach integrates thermodynamic structure, statistical validation, and predictive modeling within a unified formulation. First, the finite-size scaling relation is treated explicitly as a physics-constrained surrogate model. The scaling exponent and coefficient are extracted directly from curated literature data using constrained nonlinear regression, ensuring physical interpretability and consistency with established thermodynamic principles.

Second, uncertainty quantification is incorporated as a core component of the framework. Bootstrap resampling is used to estimate confidence intervals for the scaling exponent, enabling statistically grounded cross-material comparison. In parallel, Gaussian Process regression is integrated to model structured residual variability and provide uncertainty-aware predictions across the nanoscale regime. Importantly, the GP component augments rather than replaces the analytical scaling law, supplying predictive confidence bounds while preserving the thermodynamic form of the governing relation.

Third, the framework enables inverse design. By solving the calibrated scaling relation for a specified operating temperature, the critical particle size required to maintain ferroelectric stability can be determined directly. This shifts the analysis from descriptive scaling characterization toward temperature-constrained stability evaluation relevant to nanoscale device design.

Fourth, the formulation is extended to include linear strain coupling, enabling construction of a two-dimensional size–strain phase map. This extension permits simultaneous consideration of geometric confinement and mechanical boundary conditions within a first-order thermodynamic approximation.

Finally, the methodology is applied consistently to both $BaTiO_3$ and $KNbO_3$, enabling quantitative comparison of confinement sensitivity and nanoscale stability limits under a common physics-informed and uncertainty-aware framework. Collectively, these elements establish a transparent, statistically validated, and computationally efficient approach for systematic evaluation of finite-size effects in ferroelectric materials.

4.2. Sensitivity and stability of the extracted scaling parameters

Given the limited availability of size-resolved experimental data in nanoscale ferroelectrics, it is essential to assess whether the extracted scaling parameters are disproportionately influenced by individual measurements. To evaluate robustness, a leave-one-out sensitivity analysis was conducted, in which the scaling model was recalibrated after sequential removal of each data point. The resulting variations in the scaling exponent remained within the bootstrap-derived confidence intervals reported earlier. No single data point produced a significant shift in the fitted exponent or altered the qualitative confinement trend. This indicates that the parameter estimates are not dominated by isolated observations. The stability of inverse-design predictions was also examined. When the scaling exponent was varied within its 95% confidence interval, the estimated room-temperature critical size shifted modestly; however, the relative ranking between materials remained unchanged. In particular, $KNbO_3$ consistently retained ferroelectric stability at smaller particle sizes than $BaTiO_3$. These results demonstrate that the principal comparative conclusions are structurally robust to reasonable parameter uncertainty. Overall, the observed scaling behaviour reflects systematic confinement-driven thermodynamic trends rather than artifacts of limited sampling.

4.3. Comparison with reported scaling behaviour

Finite-size effects in ferroic nanostructures have been extensively investigated through thermodynamic modeling, phase-field simulations, and experimental characterization. Early analytical treatments demonstrated that geometric confinement introduces surface-energy and depolarization-field contributions that systematically reduce the transition temperature in nanoscale particles [1–3]. Landau–Ginzburg–Devonshire (LGD)-based analyses further established intrinsic finite-size stability relations linking characteristic dimension, polarization energetics, and phase transition behaviour [4–6]. These formulations predict monotonic suppression of T_c with decreasing size, typically governed by surface-to-volume considerations and electrostatic boundary effects. Subsequent phase-field and mesoscale simulations highlighted the role of polarization gradients, domain topology, strain coupling, and electrostatic boundary conditions in shaping size-dependent phase behaviour [7, 8, 11, 12]. These studies demonstrated that confinement-induced suppression is robust across geometries but quantitatively sensitive to strain state and boundary conditions. Experimental investigations of $KNbO_3$, $BaTiO_3$, and related perovskite systems further confirmed measurable size-dependent reductions in dielectric and ferroelectric response in nanoparticles and fine-grained ceramics [19–21]. To position the present regression-derived scaling parameters within this broader literature, representative prior studies relevant to confinement-driven transition-temperature shifts are summarized in **Table 3**. Where available, the effective scaling form is indicated. It should be noted that most classical thermodynamic and analytical studies derive intrinsic size-dependence relations but do not explicitly extract regression-based power-law exponents from compiled datasets.

As summarized in **Table 3**, a broad body of theoretical, computational, and experimental literature consistently reports suppression of the transition temperature under geometric confinement across ferroic systems. While many analytical treatments imply effective inverse-dimension scaling behaviour (corresponding to exponents of order unity under certain limits), explicit regression-based extraction of scaling exponents from curated datasets is rarely performed. Within this established framework, the present regression-derived exponents ($n \approx 1.59$ for $BaTiO_3$ and $n \approx 1.40$ for $KNbO_3$) fall squarely within the physically expected 1–2 regime commonly associated with confinement-dominated phase suppression in ferroic nanostructures. The slightly larger exponent obtained for $BaTiO_3$ indicates stronger sensitivity to dimensional confinement relative to $KNbO_3$, consistent with its steeper suppression profile observed in Section 3. Importantly, the contribution of the present study is not the proposal of a new scaling law, but rather the systematic extraction of material-specific scaling parameters within a unified regression framework, together with explicit statistical confidence intervals. Earlier theoretical and experimental works primarily reported qualitative trends or model-derived functional dependencies without providing uncertainty-quantified parameter estimates. By integrating thermodynamic structure with bootstrap resampling and Gaussian Process–based uncertainty quantification, the present approach enables statistically transparent cross-material comparison while preserving physical interpretability. This combination of mechanistic grounding and uncertainty awareness distinguishes the present framework from earlier treatments of nanoscale ferroelectric phase stability and provides a reproducible pathway for extracting confinement sensitivity parameters from heterogeneous literature datasets.

Table 3. Reported finite-size scaling behavior in representative ferroic systems.

Reference	Material/system	Geometry	Approach	Reported effective scaling behavior	Explicit n reported?
Chattopadhyay et al. [1]; Zhang et al. [2]; Michael et al. [3]	Ferroelectric nanoparticles	Nanoparticles	Thermodynamic/ analytical	Monotonic T_c suppression under confinement	Not explicitly fitted
Akdogan and Safari [4]; Morozovska et al. [5,6,10]	$PbTiO_3$ and ferroic nanoparticles	Nanocrystals	LGD-based modeling	Intrinsic size-dependent stability shift; inverse-dimension tendency	Not explicitly fitted
Mangeri et al. [7]; Eliseev et al. [8]; Huang et al. [11]; Pavlenko et al. [12]	Ferroelectric nanoparticles, films, nanowires	Confined geometries	Phase-field/mesoscale modeling	Thickness- and size-dependent transition behavior	Not explicitly fitted
Dong et al. [9]	Ferroic nanomaterials	Nanoparticles	Analytical theoretical model	Explicit 1/d dependence of critical temperature	n = 1 (theoretical form)
Ge et al. [19]; Ivanov [20]; Zaman [21]	$KNbO_3$/$BaTiO_3$ systems	Nanoparticles/ Ceramics	Experimental	Measurable size-dependent dielectric and ferroelectric suppression	Not explicitly fitted
Present work	$BaTiO_3$	Compiled nanoparticle dataset	Constrained regression + UQ	Power-law suppression	n = 1.59 (95% CI: 1.43–1.72)
Present work	$KNbO_3$	Compiled nanoparticle dataset	Constrained regression + UQ	Power-law suppression	n = 1.40 (95% CI: 1.31–1.52)

4.4. Applicability limits of the scaling framework

The adopted power-law formulation captures the dominant confinement-driven suppression behavior within the investigated nanoscale regime. However, its applicability is bounded by well-established physical considerations. At extremely small particle sizes (approaching ~1–2 nm), additional effects such as structural reconstruction, discrete lattice distortions, quantum confinement, and non-continuum electrostatics may become significant. In these regimes, continuum thermodynamic descriptions may lose validity, and atomistic simulations or higher-order free-energy formulations would be required to accurately describe phase stability. The present framework also assumes approximately isotropic particle geometries and spatially homogeneous strain conditions. In realistic systems, shape anisotropy, faceting, defect distributions, compositional gradients, and heterogeneous interfaces can modify the effective scaling response. Furthermore, near the bulk limit, deviations from ideal power-law behavior may arise due to internal stresses or microstructural inhomogeneities not explicitly incorporated in the surrogate formulation. Accordingly, the proposed model should be interpreted as a mesoscale thermodynamic description applicable within the experimentally accessible nanoscale range considered here. Integration with first-principles methods or phase-field simulations may further refine predictive capability beyond this regime.

5. Limitations and future directions

The proposed framework provides a statistically grounded and computationally efficient methodology for finite-size scaling analysis in ferroelectric nanostructures. Nevertheless, several limitations define opportunities for further development.

First, the dataset is compiled from previously published studies conducted under varying synthesis conditions, geometries, and measurement protocols. Although careful standardization and statistical resampling were implemented, some variability inevitably reflects differences in experimental environments rather than purely intrinsic material behavior. Systematically generated datasets under controlled conditions would further enhance quantitative precision and reduce cross-study variability.

Second, the surrogate formulation captures thermodynamic scaling behavior at a mesoscopic level but does not explicitly resolve microscopic features such as domain-wall structures, polarization textures, or atomistic surface reconstruction. These effects are implicitly reflected in the observed scaling trends but are not directly modelled. Coupling the present framework with phase-field simulations or first-principles calculations could provide deeper insight into the microscopic origins of the extracted scaling exponents.

Third, the analysis assumes fixed bulk Curie temperatures for each material. In practice, T_{bulk} may vary with composition, defect density, processing history, or internal stress. Incorporating composition- or defect-dependent bulk parameters would broaden applicability to more complex and engineered materials systems.

Finally, the strain coupling introduced in the two-dimensional phase map is treated within a linear approximation. While appropriate for moderate strain magnitudes, higher-order electromechanical interactions may become relevant under larger deformation. Extending the formulation to include nonlinear strain terms would provide a more comprehensive description of confinement–mechanical interplay. These limitations do not diminish the validity of the present results; rather, they delineate clear pathways for extending the framework toward greater physical resolution and predictive capability. The current study establishes a statistically robust foundation that can be systematically enriched through expanded datasets and multiscale modeling integration.

6. Conclusion

This study presents a physics-informed surrogate framework for analysing finite-size suppression of the Curie temperature in ferroelectric nanostructures.

By integrating a thermodynamically motivated scaling relation with statistical validation and uncertainty quantification, the work establishes a structured and physically interpretable methodology for evaluating confinement-driven phase stability. Finite-size scaling behavior in $BaTiO_3$ and $KNbO_3$ was examined using curated literature-derived datasets. The scaling exponent was extracted through constrained nonlinear regression, and its robustness was assessed via bootstrap resampling, yielding statistically grounded confidence intervals despite the limited size of available experimental data. Gaussian Process regression was further incorporated to model residual variability and provide uncertainty-aware predictions across the nanoscale regime, strengthening reliability assessment of the surrogate formulation. Beyond forward prediction, the framework enables inverse evaluation of nanoscale stability limits by estimating the critical particle size required to maintain ferroelectric order at a specified operating temperature. Extension of the formulation to include linear strain coupling produced a two-dimensional size–strain stability map, illustrating how moderate mechanical loading can partially offset confinement-induced suppression within a first-order approximation. Comparative analysis reveals clear material-dependent differences in confinement sensitivity and nanoscale stability windows between $BaTiO_3$ and $KNbO_3$ under a unified modeling and uncertainty framework. These findings underscore that finite-size scaling is intrinsically material-specific and should be evaluated through physically grounded and statistically validated parameter extraction schemes. Overall, the proposed methodology bridges classical thermodynamic scaling concepts with modern uncertainty-aware surrogate modeling in a computationally efficient and transparent manner. While not intended to replace atomistic or phase-field simulations, it provides an adaptable tool for systematic evaluation and rational design of nanoscale ferroelectric and related ferroic materials. A complete step-by-step description of the algorithmic implementation of the proposed physics-informed scaling framework is provided in **Appendix A**.

Funding: This work received no external funding.

Institutional review board statement: This study does not involve human participants or animals. Ethical approval was therefore not required.

Informed consent statement: Not applicable.

Data availability statement: The datasets analysed during the current study were compiled from publicly available literature sources, as cited in the manuscript. The processed dataset and computational scripts used for scaling analysis, bootstrap resampling, and phase mapping are available from the corresponding author upon reasonable request.

Conflict of interest: The author declares no competing financial or non-financial interests related to this work.

AI use statement: Grammarly was used to assist in improving grammar, readability, and clarity of the manuscript. No AI tools were used for data generation, analysis, scientific interpretation, or formulation of the research results. All scientific content, modeling, and analysis were developed by the author.

References

1. Chattopadhyay S, Ayyub P, Palkar VR, et al. Finite-size effects in antiferroelectric $PbZrO_3$ nanoparticles. Journal of Physics: Condensed Matter. 1997; 9: 8135.
2. Zhang L, Zhong WL, Wang CL, et al. Finite-size effects in ferroelectric solid solution $Ba_xSr_{1-x}TiO_3$. Journal of Physics D: Applied Physics. 1999; 32: 546.
3. Michael T, Trimper S, Wesselinowa JM. Size effects on static and dynamic properties of ferroelectric nanoparticles. Physical Review B: Condensed Matter and Materials Physics. 2007; 76: 094107.
4. Akdogan EK, Safari A. Thermodynamic theory of intrinsic finite-size effects in $PbTiO_3$ nanocrystals. I. Nanoparticle size-dependent tetragonal phase stability. Journal of Applied Physics. 2007; 101: 064114.
5. Morozovska AN, Glinchuk MD, Eliseev EA. Phase transitions induced by confinement of ferroic nanoparticles. Physical Review B: Condensed Matter and Materials Physics. 2007; 76: 014102.
6. Morozovska AN, Eliseev EA, Glinchuk MD. Size effects and depolarization field influence on the phase diagrams of cylindrical ferroelectric nanoparticles. Physica B: Condensed Matter. 2007; 387(1–2): 358–366.
7. Mangeri J, Espinal Y, Jokisaari A, et al. Topological phase transformations and intrinsic size effects in ferroelectric nanoparticles. Nanoscale. 2017; 9(4): 1616–1624.
8. Eliseev EA, Fomichov YM, Kalinin SV, et al. Labyrinthine domains in ferroelectric nanoparticles: Manifestation of a gradient-induced morphological transition. Physical Review B. 2018; 98: 054101.
9. Dong P, Li W, Zhao Z, et al. Theoretical prediction of size and dimension dependent critical temperature for ferroelectric, ferromagnetic and superconductive nanomaterials. Journal of Physics and Chemistry of Solids. 2021; 154: 110043.
10. Morozovska AN, Eliseev EA, Glinchuk MD, et al. Analytical description of the size effect on pyroelectric and electrocaloric properties of ferroelectric nanoparticles. Physical Review Materials. 2019; 3: 104414.
11. Huang CW, Chen ZH, Chen L. Thickness-dependent evolutions of domain configuration and size in ferroelectric and ferroelectric-ferroelastic films. Journal of Applied Physics. 2013; 113: 094101.
12. Pavlenko MA, Di Rino F, Boron L, et al. Phase diagram of a strained ferroelectric nanowire. Crystals. 2022; 12(4): 453.
13. Zhu D, Mangeri J, Wang R, et al. Size, shape, and orientation dependence of the field-induced behavior in ferroelectric nanoparticles. Journal of Applied Physics. 2019; 125: 134102.
14. Kushwaha AK, Khadka R, Keblinski P. Surface-Induced effects in ferroelectric $BaTiO_3$ thin films. Surfaces and Interfaces. 2025; 56: 105589.
15. Li C, Qin H, Zhou Y, et al. Strain-Induced Polar Interfaces in Ferroelectric Polymer Nanocomposites. Advanced Functional Materials. 2025; 35(35): 2421825.
16. Cao L, Xie D, Guo M, et al. Size and shape effects on Curie temperature of ferromagnetic nanoparticles. Transactions of Nonferrous Metals Society of China. 2007; 17(6): 1451–1455.
17. Penny C, Muxworthy AR, Fabian K. Mean-field modelling of magnetic nanoparticles: The effect of particle size and shape on the Curie temperature. Physical Review B. 2019; 99: 174414.
18. Huang J, Aghabozorgi F, Brock S. Quantum Saturation of Magnetoelectric Coupling in Fe_3O_4 Nanoparticles. arXiv preprint. 2025; arXiv:2509.24131.
19. Ge H, Huang Y, Hou Y, et al. Size dependence of the polarization and dielectric properties of $KNbO_3$ nanoparticles. RSC Advances. 2014; 4(44): 23344–23350.
20. Ivanov M. Grain Size Effect on Dielectric Properties of Ferroelectrics and Relaxors [PhD Thesis]. Vilnius University; 2014.
21. Zaman T. Study of Structural, Dielectric and Ferroelectric Properties of Lead-Free $BaTiO_3$-$K_{0.5}Na_{0.5}NbO_3$ Ceramics. Bangladesh University of Engineering and Technology; 2016.
22. Rørvik PM. Synthesis of Ferroelectric Nanostructures [PhD Thesis]. Norwegian University of Science and Technology; 2008.
23. Blanco AA. Nanomaterial Composites Based on Potassium Hexaniobate, Perovskites, and Iron Triazole Spin Crossover Complexes [PhD Thesis]. University of New Orleans; 2020.
24. Khorsand Zak A, Yazdi ST, Abrishami ME, et al. A review on piezoelectric ceramics and nanostructures:

Fundamentals and fabrications. Journal of the Australian Ceramic Society. 2024; 60(3): 723–753.
25. Alhada-Lahbabi K, Deleruyelle D, Gautier B. Machine learning surrogate model for acceleration of ferroelectric phase-field modeling. ACS Applied Electronic Materials. 2023; 5(7): 3894–3907.
26. Alhada-Lahbabi K, Deleruyelle D, Gautier B. Machine learning surrogate for 3D phase-field modeling of ferroelectric tip-induced electrical switching. npj Computational Materials. 2024; 10: 197.
27. Alhada-Lahbabi K, Deleruyelle D, Gautier B. Reinforcement Learning-Assisted Ferroelectric Domain Wall Design Using a Machine Learning Phase-Field Surrogate. ACS Applied Electronic Materials. 2025; 7(3): 1130–1141.
28. Smith BR, Pant B, Liu Y, et al. Physics-informed models of domain wall dynamics as a route for autonomous domain wall design via reinforcement learning. Digital Discovery. 2024; 3(3): 456–466.
29. Fassi Y, Heiries V, Boutet J, et al. Toward physics-informed machine-learning-based predictive maintenance for power converters—A review. IEEE Transactions on Power Electronics. 2023; 39(2): 2692–2720.
30. Qin S. Physical-Informed Networks for Multi-Modal Spectroscopies [PhD Thesis]. Lehigh University; 2025.
31. Xu K, Yang L, Wang J, et al. Design of high energy storage ferroelectric materials by phase-field simulations. Journal of Materials Informatics. 2025; 5(2): 24.
32. Casals B, Nataf GF, Salje EKH. Avalanche criticality during ferroelectric/ferroelastic switching. Nature Communications. 2021; 12: 345.
33. Gómez-Cortés JF, Nó ML, López-Ferreño I, et al. Size effect and scaling power-law for superelasticity in shape-memory alloys at the nanoscale. Nature Nanotechnology. 2017; 12(8): 790–796.
34. Tasneem N, Yousry YM, Tian M, et al. A Janovec-Kay-Dunn-Like Behavior at Thickness Scaling in Ultra-Thin Antiferroelectric ZrO_2 Films. Advanced Electronic Materials. 2021; 7(11): 2100485.
35. Kalinin SV, Eliseev EA, Morozovska AN. Adsorption of ions from aqueous solutions by ferroelectric nanoparticles. Physical Review Applied. 2025; 23: 014081.
36. Shi Y, Huang Z, Lin Y, et al. In situ formation of carbon-based tribo-films via engineered composite design for enhanced anti-adhesion performance in metallic contacts. Wear. 2025; 580–581: 206271.
37. Zhou Q, Jiao Z, Huang Z, et al. Wear-resistant CrCoNi nanocrystalline film via friction-driven surface segregation. Acta Materialia. 2024; 279: 120299.
38. Zhou Q, Xia Q, Li Q, et al. Microstructure, mechanical and tribological properties of NbMoWTaAg refractory high entropy films with nano-layered self-organization. Tribology International. 2024; 198: 109888.

Appendix A. Algorithmic implementation of the physics-informed scaling framework

This appendix summarizes the computational workflow used for finite-size scaling analysis, uncertainty quantification, and inverse design.

Appendix A.1. Finite-size scaling model

The thermodynamic scaling relation is defined as:

$$T_c(d) = T_{\text{bulk}} - \frac{A}{d^n} \tag{A1}$$

where:

- T_{bulk} is the bulk Curie temperature,
- A is the surface-related scaling coefficient,
- n is the finite-size exponent,
- d is the particle size.

When strain coupling is included, the model becomes:

$$T_c(d, \varepsilon) = T_{\text{bulk}} - \frac{A}{d^n} + k\varepsilon \tag{A2}$$

where ε denotes epitaxial strain and k is the strain-coupling coefficient.

Appendix A.2. Parameter estimation procedure

The scaling parameters A and n are estimated using constrained nonlinear least-squares regression.

The objective function is:

$$L(A,n) = \frac{1}{N}\sum_{i=1}^{N}\left[T_{c,i}^{\text{obs}} - \left(T_{\text{bulk}} - \frac{A}{d_i^n}\right)\right]^2 \tag{A3}$$

where N is the number of data points.

Algorithm A1 Physics-informed finite-size scaling parameter estimation using constrained nonlinear regression

```
1. Input:
    ○ Particle sizes $d_i$
    ○ Measured transition temperatures $T_{c,i}^{\text{obs}}$
    ○ Known bulk temperature $T_{\text{bulk}}$
2. Initialization:
    ○ Set initial parameter guesses $A_0, n_0$
3. Optimization:
    ○ Minimize $L(A,n)$ using nonlinear regression (e.g., Levenberg–Marquardt algorithm)
    ○ Apply bounded constraints to enforce $A > 0$, $n > 0$
4. Output:
    ○ Estimated parameters $A_{\text{est}}$, $n_{\text{est}}$
```

Appendix A.3. Bootstrap uncertainty estimation

To estimate confidence intervals for the scaling exponent:

1. For $b = 1, \ldots, B$ bootstrap iterations:
    - Randomly resample the dataset with replacement.
    - Refit parameters $A^{(b)}$, $n^{(b)}$.
2. Construct the empirical distribution of $n^{(b)}$.
3. Compute the confidence interval:

$$n_{\text{CI}} = [\text{Percentile}_{2.5\%},\ \text{Percentile}_{97.5\%}] \tag{A4}$$

This procedure provides statistically defensible bounds for the extracted exponent.

Appendix A.4. Critical size determination (inverse design)

To determine the particle size required to achieve a target operating temperature T^*, the following condition is solved:

$$T_c(d^*) = T^* \tag{A5}$$

Substituting Equation (A1):

$$T_{\text{bulk}} - \frac{A_{\text{est}}}{(d^*)^{n_{\text{est}}}} = T^* \tag{A6}$$

Root finding is performed using a bracketing method (e.g., Brent's algorithm).

Algorithm A2 Inverse design algorithm for critical particle size determination

```
1. Define the function:
       $f(d) = T_c(d) - T^*$                (A7)
2. Identify a bracketing interval $[d_{\min},\ d_{\max}]$
3. Solve $f(d^*) = 0$
```

The resulting d^* represents the critical particle size required to maintain ferroelectric stability at temperature T^*.

Appendix A.5. Two-dimensional phase mapping

For size–strain mapping:

1. Generate a mesh grid over particle size d and strain ε.
2. Evaluate Equation (A2) over the grid.
3. Construct a contour map of $T_c(d,\varepsilon)$.
4. Identify the stability region where:

$$T_c(d,\varepsilon) \geq T^* \tag{A8}$$

This procedure produces a two-dimensional nanoscale stability landscape under combined geometric and mechanical constraints.

Appendix A.6. Summary of computational workflow

1. Input experimental size–temperature dataset.
2. Fit physics-informed scaling model (Equation (A1)).
3. Perform bootstrap uncertainty estimation (Equation (A4)).
4. Validate scaling behavior via log–log transformation.
5. Determine critical size using root finding (Equations (A6) and (A7)).
6. Extend to size–strain phase mapping (Equations (A2) and (A8)).